Evaporation of femtoliter sessile droplets monitored with nanomechanical sensors

5 AUTHORS, INCLUDING:

Julien Arcamone

Atomic Energy and Alternative Energies Com…

67 PUBLICATIONS   **418** CITATIONS

SEE PROFILE

Erik Dujardin

French National Centre for Scientific Research

104 PUBLICATIONS   **6,437** CITATIONS

SEE PROFILE

Gemma Rius

Nagoya Institute of Technology

66 PUBLICATIONS   **449** CITATIONS

SEE PROFILE

Francesc Pérez-Murano

Spanish National Research Council

245 PUBLICATIONS   **2,640** CITATIONS

SEE PROFILE

Evaporation of Femtoliter Sessile Droplets Monitored with Nanomechanical Mass Sensors

Julien Arcamone,[†] Erik Dujardin,[‡] Gemma Rius,[†] Francesc Pérez-Murano,[†] and Thierry Ondarçuhu*,[‡]

CNM-IMB (CSIC), Campus UAB, 08193 Bellaterra, Barcelona, Spain, and NanoSciences Group, CEMES-CNRS, 29 rue Jeanne Marvig, 31055 Toulouse cedex 4, France

Received: July 20, 2007; In Final Form: August 30, 2007

We present a time-resolved study of the evaporation in air of minuscule sessile droplets deposited by nanodispensing techniques. Highly sensitive nanomechanical resonators are designed to monitor in time the mass variation of evaporating liquid droplets. The precision of the measurement setup enables the study of droplets with diameters in the 1 μm range, which correspond to volumes of femtoliters and smaller, 9 orders of magnitude smaller than most of presently published data. Experimental data are compared with macroscopic models.

1. Introduction

For several decades, the evaporation of sessile droplets has attracted a lot of attention because of its implication in everyday life and in many industrial processes. The first theoretical description of droplet evaporation, given by Maxwell more that 100 years ago, considered that the evaporation rate is governed by the diffusion of molecules in the gas phase.[1] Since then, many refinements have been proposed to better describe the basic modes of evaporation of sessile droplets depending on the wetting properties of the substrate.[2−12] Experimentally, these modes have been evidenced by direct observation of sizes and contact angles of droplets in the microliter range corresponding to millimetric dimensions.

However, the recent progress of nanosciences has been accompanied by the development of methods based on the manipulation of much smaller quantities of liquids. For instance, the scaling down of micro- to nanofluidics or the emergence of liquid lithography methods such as ink jet[13] or liquid nanodispensing techniques[14,15] leads to situations in which evaporation becomes a dominant factor with contrasted consequences. Indeed, microfluidic systems can be activated by evaporation-based pumping mechanisms,[16] and evaporation-driven concentration of small volumes of solution or suspensions provides a new tool for the kinetic exploration of liquids.[17] Interestingly, evaporation induces compensation flux[18,19] that may be finely controlled for the local self-assembly of nanoparticles[20] or macromolecules such as DNA.[21] Conversely, when subfemtoliter quantities of liquids are dispensed from a reservoir onto a substrate, the evaporation of open reservoirs becomes the limiting technological factor that needs to be obviated.[15] It is therefore essential to extend the study the evaporation of droplets down to the submicrometer scale, that is, to subfemtoliter volumes, and to investigate whether the models derived from macroscopic arguments remain valid down to these sizes. In practice, this downscaling by 9 orders of magnitude in volume from most published data requires the combination of two newly

developed nanoscale techniques described hereafter: one to produce the droplet and one to monitor its weight evolution in real time.

Although producing and manipulating droplets with diameters down to tens of micrometers is routinely achieved with a number of techniques, such as ink jet printing[13] or micromachined quill writing,[22] the delivery of submicrometer droplets remains challenging. In this size regime, the most effective method to date is the liquid nanodispensing (NADIS) technique, in which a small quantity of liquid is transferred from an on-chip reservoir onto the substrate through a small aperture drilled at the apex of an atomic force microscope (AFM) tip by focused ion beam. In particular, it was shown that NADIS tips with optimized shape and surface functionalization can be used to deposit large arrays of droplets with diameters as small as 75 nm (100 zL).[15] These performances combined with the high positioning precision capabilities of AFM-based surface nanopatterning methods make of NADIS the ideal technique for evaporation studies at micrometer scale.

Monitoring the evaporation process of submicrometer droplets cannot be achieved by standard optical microscopy techniques, which prompted us to measure in real time the mass of the droplet during evaporation. Several classical microelectromechanical systems could be envisioned, among which quartz microbalances or cantilevers would be the most promising. Nevertheless, quartz microbalances (QCM) do not provide enough sensitivity, limiting evaporation studies to microliter droplets.[23,24] Cantilevers can reach very high mass resolution, but quantitative measurements on liquids are difficult. Notwithstanding, a new technique using cantilever bending caused by a droplet deposited on the cantilever[25] recently allowed monitoring of evaporation of droplets as small as 40 pL.[26] These techniques are therefore not adequate for our purpose. Consequently, we designed a new type of sensor based on recently developed quad beam resonators, the performances of which match the requirements of the evaporation experiments in the femtoliter (i.e., submicrometer) range.

In the following, we show that the unique combination of ultrasensitive mass sensors with liquid nanodispensing techniques allows the study of evaporation of femtoliter sessile droplets that are 9 orders of magnitude smaller than previously

* Corresponding author. Phone: (33) 5 62 25 78 38. Fax: (33) 5 62 25 79 99. E-mail: ondar@cemes.fr.
† CNM-IMB.
‡ CEMES-CNRS.

Evaporation of Sessile Droplets

J. Phys. Chem. B, Vol. 111, No. 45, 2007 **13021**
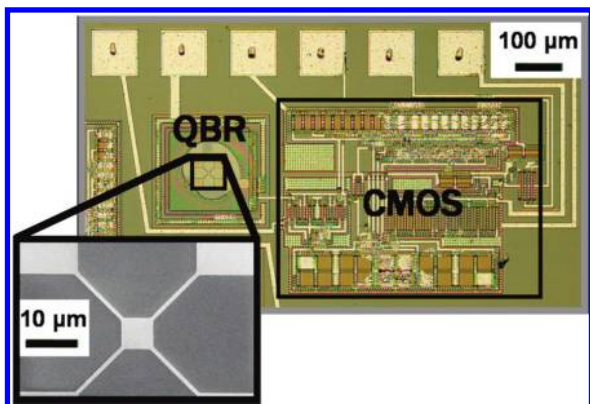
Figure 1. Optical image of a CMOS-integrated QBR. Inset: SEM image of a QBR, the dimensions of which are plate area, $6 \times 6 \ \mu m^2$; beam width, 600 nm; beam length, 13.5 μm; and QBR thickness, 450 nm.

reported data. After a presentation of our approach (Section 2), we report results obtained with glycerol and discuss them in the framework of existing models (Section 3).

2. Experimental Methods

In this section, we first describe the design and calibration of the quad-beam nanomechanical resonators used as mass sensors and compare their performances to those of cantilevers and quartz-crystal microbalances. The procedures for dispensing droplets onto the resonators and the monitoring of the decrease of the droplets' masses during the evaporation process are then discussed.

2.1. Nano-/Micromechanical Resonators for Mass Sensing.
2.1.1. Device Characteristics. The nanomechanical device is a polysilicon quad-beam resonator (QBR) (see Figure 1, inset) which consists of four beams supporting a suspended central plate that can be vibrated at its resonance frequency, where the device is highly sensitive to small added mass.[27] The resonance frequency, f_0, of the fundamental out-of-plane flexural mode depends upon the material properties and geometrical dimensions of the resonator. It is calculated using the Rayleigh–Ritz method.[28] Then,

$$ f_0 \approx \frac{1}{2\pi} \sqrt{\frac{Ebh^3}{m_{EFF}l^3}} \qquad (1) $$

with

$$ m_{EFF} = m_P + \frac{33}{140} m_B \qquad (2) $$

where E is the Young's modulus of the structural material; and l, b, and h are, respectively, the length, the width, and the thickness of the four beams of the QBR. The effective mass of the resonator m_{EFF} is given by eq 2, where m_P and m_B are the mass of the central plate and that of a beam respectively.

The dimensions of the devices have been adequately chosen so that the QBR has resonance frequencies in the MHz range (limit set by the detection setup) and a sensitivity to point mass accretion on the order of 100 ag (10^{-16} g)/Hz. To fulfill these requirements, QBRs typically have the following dimensions: plate width and beam length around 10 μm, plate thickness and beam width in the submicrometer range.

Moreover, the QBR design remains mostly insensitive to (i) the adsorbate stiffness[29] and (ii) the induced surface stress[30] when depositing a punctual mass on the central plate and

operating it in the fundamental out-of-plane flexural mode. Interestingly, since the plate can be considered as rigidly flat, it uniformly undergoes the same deflection when operated in that mode so that the position of the adsorbate on the plate does not affect the resonance frequency shift.[27,31] In such operating conditions, the mass loading effect is mechanically dominant over stiffness (i.e., spring constant) variations and is the single factor causing a resonance frequency downshift. Therefore, we can express the corresponding sensitivity to point mass accretion, S_P^0, of the fundamental out-of-plane flexural mode as[32]

$$ S_P{}^0 \approx 2 \frac{m_{EFF}}{f_0} \qquad (3) $$

In addition to their potential high mass sensitivity, QBRs provide a large active area that is particularly suited for mass measurements in air of small quantities of either liquid or solid compounds. In the context of evaporation measurements of droplets, the alignment of the nanodroplet dispensing probe with QBR sensors is considerably easier than, for example, with narrow bridges or cantilevers.

2.1.2. Device Fabrication. QBRs are defined by electron-beam lithography (eBL) on prefabricated CMOS substrates. In our postprocessing approach,[33] CMOS circuits are first fabricated according to a standard technology. Then, dedicated areas formed by polysilicon on field oxide are selectively patterned by eBL using a poly(methyl methacrylate) (PMMA) resist, deposition of a 32-nm-thick Al layer, and lift-off. Al patterns serve as an etch mask for the subsequent pattern transfer to polysilicon by reactive ion etching.

Finally, the vibrating structure is released by buffered fluorhydric acid. A 5-μm-thick SU8 layer is used to protect the CMOS circuits during this wet etching. In this way, monolithically integrated nanomechanical devices with lateral resolutions down to 200 nm are routinely fabricated.

2.1.3. Electronic Detection Scheme. The mechanical oscillations of QBR are converted into an electrical signal using a capacitive detection scheme. This approach provides a favorable tradeoff between simplicity of implementation, displacement resolution, and system portability, and its up-scaling to the parallel operation of multiple arrayed devices is straightforward. In the specific case of liquid sensing, the capacitive detection scheme has the advantage of being noninvasive with respect to evaporation processes.

To optimize the electrical response, QBRs have been monolithically integrated with a specific CMOS circuitry designed for reading out the capacitive current produced at resonance.[34] This improves the readout quality by drastically reducing the parasitic output capacitances and enables "on-chip" signal amplification and conditioning.

Figure 2 depicts characteristic magnitude and phase responses of an unloaded QBR operated in air. The resonance frequency, f_U, can be tuned down by increasing the applied dc voltage $V_{IN,DC}$ (this is the so-called spring-softening effect[35]). For $V_{IN,DC}$ larger than about 20 V, the QBR exhibits a nonlinear behavior evidenced by the dissymmetry of the responses. This nonlinearity originates in the reduced thickness of the plates (ca. 450 nm), which sets the critical oscillation amplitude[36] in the direction of vibration. The resulting sharpness in the output signals could potentially be used to further enhance the mass sensitivity.[37]

2.1.4. Calibration of the Resonators. To use resonators as reliable mass sensors, a precise calibration procedure must be performed; therefore, the resonance frequency shift was mea-

13022 *J. Phys. Chem. B, Vol. 111, No. 45, 2007*

Arcamone et al.
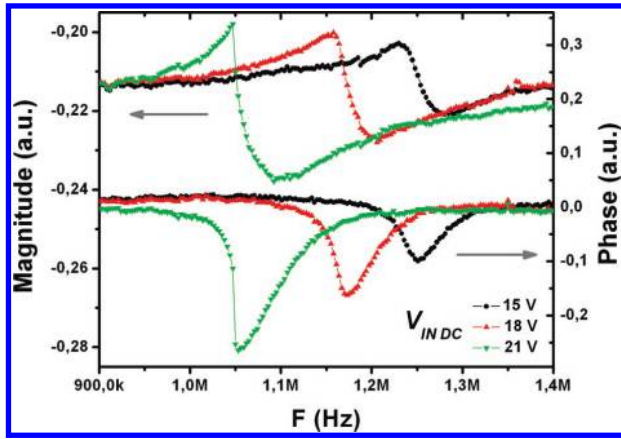
Figure 2. Calibrated resonance spectra in air of a QBR for several bias voltages ($V_{IN,DC}$) and a fixed excitation voltage, $V_{IN,AC} = 0.9$ V.
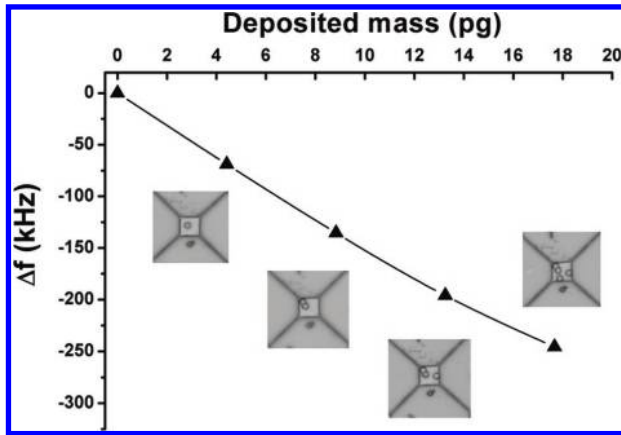

Figure 3. Calibration curve of the QBR. The frequency shift is reported as a function of the loaded mass corresponding to one to four silica beads. The images show the corresponding situations.

sured for a QBR loaded with calibrated silica beads (diameter 1.57 ± 0.06 μm, Duke Scientific Corporation) so as to cover the anticipated range of droplet weights. The manipulation of the beads was performed under an optical microscope using a micromanipulation setup (the Micromanipulator Inc). Individual beads were deposited onto the central plate of a QBR with micropipettes with an external diameter in the 1 μm range, obtained from glass capillaries using a micropipette puller (Narishige). The corresponding shift in the resonance frequency was measured using the electronic setup described above.

First, an individual glass bead was added and removed several times to assess the reproducibility of the measurement. We found a maximum deviation of 1%. Specific attention was brought to detect a possible influence of the bead position on the QBR central plate. In agreement with mechanical predictions, no influence of the position was observed, even for very off-centered loads, thus confirming the suitability of QBR devices as punctual mass sensors.

Similar loading procedures of two, three, and four beads on the QBR allowed exploring the entire expected droplet mass range. The results, reported in Figure 3, provide the calibration curve of the QBR, which was used for subsequent evaporation curves. The relationship of frequency shift vs deposited mass is linear up to ca. 10 pg, beyond which it starts to saturate. This curve was fitted with a mathematical function that was subsequently inverted to give a conversion function between frequency shift and mass.

For a deposited mass smaller than 10 pg, the calibration curve follows a linear trend. The slope of this curve, also called
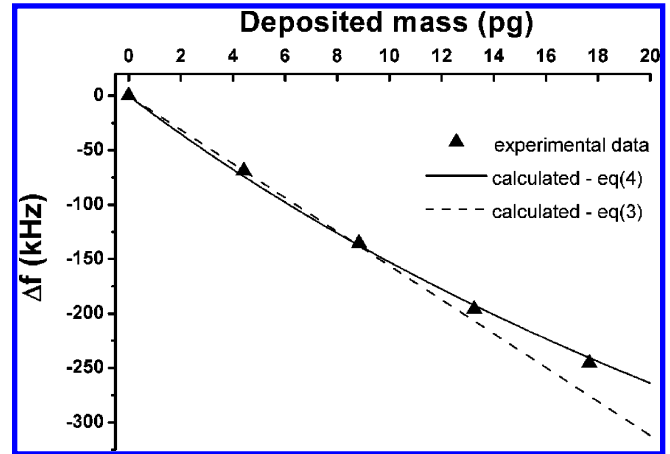
Figure 4. Comparison between the experimental data of Figure 3 and the theoretical curves given by eqs 3 and 4.

TABLE 1: Comparison between Nanocantilevers, Commercial QCM, and Silicon QBR in Terms of Areal and Point Mass Accretion Sensitivities, Frequency Resolution in Air, and Resulting Mass Resolution in Air

device	S_{AREAL} (g cm^{-2} Hz^{-1})	S_P (g Hz^{-1})	Δf_{MIN} (Hz)	Δm_{MIN} (pg)
nanocantilevers[38]		1.4×10^{-21}	100	1.4×10^{-7}
QCM	1.23×10^{-8}	1.84×10^{-8}	0.005	92
Si QBR	1.8×10^{-10}	6.4×10^{-17}	1000	0.064

responsivity, is the inverse of the sensitivity to point mass accretion S_P (given by eq 3 replacing f_0 by f_U). For small variations around the unloaded resonance frequency, S_P is estimated from Figure 3 around 6.4×10^{-17} g Hz^{-1} (i.e., 64 ag/Hz).

However, for a larger deposited mass, the calibration curve deviates from the linear trend (Figure 3). The fact that the responsivity ($1/S_P$) cannot be considered constant anymore but tends to decrease as f increases leads to a saturation regime and reveals that the deposited mass reaches a significant fraction of the plate effective mass. Therefore, the resonance frequency variation with mass can be written as

$$f_{RES} = f_U \sqrt{\frac{m_{EFF\_P}}{m_{EFF\_P} + m_{DEPOSITED\_PUNCTUAL}}} \qquad (4)$$

where f_U is the initial unloaded resonance frequency (set by the level of $V_{IN,DC}$), m_{EFF_P} is the effective mass of the unloaded resonator, and $m_{DEPOSITED\_PUNCTUAL}$ is the quantity of deposited mass. m_{EFF_P} can be calculated from eq 2.

In Figure 4, the experimental data from Figure 3 are compared to the expressions given by eqs 3 and 4. The theoretical curve given by eq 4 is precisely fitted to the data by adjusting the effective mass of the resonator m_{EFF_P} to 38 pg, in very good agreement with the nominal value of 42 pg, derived from the QBR dimensions measured by SEM.

2.1.5. Performances of QBR Compared to QCM and Cantilever-Based Devices. Upon the basis of the calibration results and assuming small deposited accretions of mass, the performances of QBRs as mass sensors can be compared to highly sensitive cantilever-based systems and to commercially available quartz-crystal microbalances. For each device, we reported in Table 1 areal, S_{AREAL}, and punctual, S_P, mass sensitivities, frequency resolution in air Δf_{MIN}, and the the resulting minimum detectable mass Δm_{MIN}, given by $\Delta m_{MIN} = \Delta f_{MIN} \times S_P$ (see Table 1).
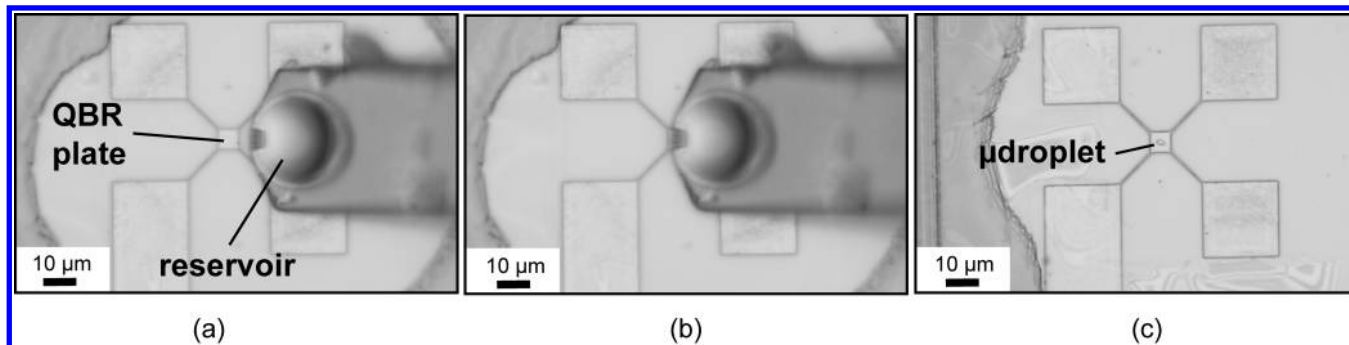
Figure 5. Optical microscope images of the deposition procedure: (a) the preloaded NADIS tip is approached from the surface; (b) the QBR is positioned under the tip with the nanopositioning table; (c) after contact, the tip is withdrawn, leaving a droplet on the surface.

Cantilevers can reach very high mass resolution: down to attogram (10^{-18} g) in air[38] and even to zeptogram (10^{-21}g) in ultrahigh vacuum conditions.[39] Nevertheless, these performances were achieved using very small cantilevers with dimensions in the submicrometer range that would make the droplet deposition experimentally hazardous. Using standard AFM cantilevers, a quantitative measurement of the mass variation by monitoring the shift in resonance frequency is difficult, since it requires an accurate value of their stiffness (which is usually not measurable) and depends on the position of the deposited droplet on the cantilever. Moreover, laser-based optical detection techniques are likely to alter the measurement, since the heat dissipated by the laser spot onto the cantilever surface would artificially accelerate the evaporation rate. Recently, a new technique using the static bending caused by surface tension and Laplace pressure exerted by a droplet on the cantilever[25] turned out to be an efficient tool to monitor evaporation droplets down to 40 pL.[26] Nevertheless, it still requires some optical measurements of droplet size, limiting the use at the 10 μm scale. The present state of the art cantilever-based sensors are therefore not adapted to quantitative measurements of liquid droplets in the micrometer range and below.

QCMs have an outstanding frequency resolution but suffer from a poor sensitivity to point mass accretion (in fact, they are usually applied as areal mass sensors; i.e., when the target accretion is uniformly deposited over the whole sensor). This technique has been used for evaporation studies of microliter droplets,[23,24] but it obviously does not provide enough sensitivity for the targeted masses of our study, which are in the pico- to femtogram range. In comparison, silicon QBRs have a poor frequency resolution but a very high sensitivity to point mass accretion. The experimental mass resolution of Si QBR is 3 orders of magnitude better than the one of commercial QCM.

QBR is therefore the most suitable technique for study of evaporation of femtoliter droplets. In addition to an adequate mass sensitivity, their main advantages are the sizes, which are compatible with our dispensing technique, and a nonperturbative detection, which does not interfere with the evaporation process. Since the objective is to monitor the mass decrease from its initial value, m_0, until about $m_0/10$, this latter value should not be less than 0.064 pg (i.e., the detection limit Δm_{MIN} in Table 1). The corresponding minimum initial diameter of the droplet is on the order of 1−2 μm, depending on the hydrophilic character of the QBR surface (hydrophobic surfaces result in larger volumes for a fixed diameter). This size sets the aperture size of the NADIS probes as described below.

2.2. Droplet Deposition by Liquid Nanodispensing. We used the NADIS technique to deposit droplets with controlled sizes on the QBR plate. An aperture, drilled by focused ion beam at the apex of a commercial AFM tip with hollow pyramidal shape, is used to transfer liquid from a reservoir drop deposited on the upper side of the AFM cantilever to the surface by mechanical contact. We have demonstrated that droplets with diameters ranging from 1 μm down to 75 nm can be delivered onto a surface by precisely tuning the hole diameter, tip surface chemistry, and deposition conditions.[15] To produce the larger droplets needed for the present evaporation study, the fabrication and deposition conditions were adapted. NADIS tips with 300-nm-wide apertures were fabricated according to the procedure reported in ref 15. Droplets deposited with as-prepared tips have a diameter in the 1 μm range. To obtain larger droplets, the outer wall of the tip was rendered highly hydrophilic by a UV−ozone cleaning. In this case, the liquid spreads on the tip outer sides, leading to droplets with diameters that can be adjusted between submicrometer and 5 μm by controlling the contact time with the QBR surface from less than 1 s up to 10 s.

Although the position of the deposited mass on the QBR does not influence its response, as demonstrated with the silica beads, an off-center positioning of a droplet could lead to liquid flowing between the QBR and the substrate and resulting in the destruction of the device by capillary adhesion. Hence, it is recommended that the droplets be positioned with a high precision at the center of the QBR. This was successfully achieved with a nanopositioning setup recently implemented under the AFM sample holder.[40] The procedure is the following: (i) The liquid-loaded NADIS tip was put on the AFM tip holder. (ii) The tip was brought close to the surface but not in contact so that both surface and cantilever were in focus (Figure 5a). (iii) The position of the sample under the tip was adjusted by moving the nanopositioning table (Figure 5b). (iv) The tip−substrate approach process was resumed and completed. (v) Upon contacting, the tip was either withdrawn immediately or left in contact with the surface for a given contact time before withdrawing. Figure 5c shows an optical image of a 1.5 μm droplet deposited on a QBR by this protocol.

Real-time droplet mass loss was monitored by measuring time-lapsed resonance curves in situ under the AFM used for depositing the droplets. A dedicated sample holder was designed to fix the printed circuit board bearing the QBR chip on the AFM nanopositioning table. All experiments were performed in ambient atmosphere with a controlled room temperature of 22 °C. The temperature on the sample holder of the AFM, measured with a thermocouple, was 26 °C. The connections to the electronic equipment were done with SMA connectors and coaxial cables (Figure 6a). Resonance curves were continuously recorded during the evaporation process and stored using a dedicated software control interface. Phase curves acquired before droplet deposition and during the evaporation process are displayed in Figure 6b. Upon droplet deposition, the resonance frequency downshifts immediately and then gradually
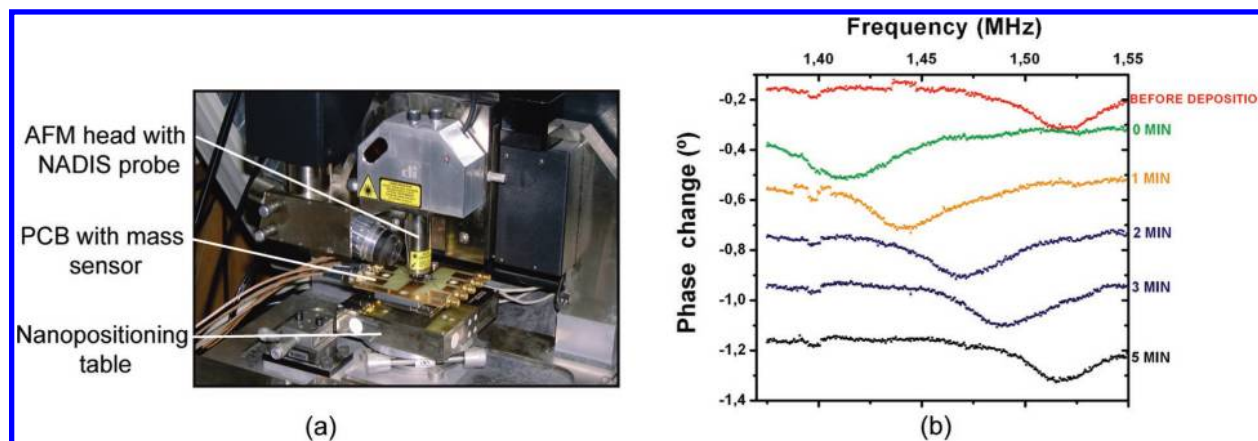
Figure 6. (a) Photograph of the setup. The printed circuit board connecting the QBR to the external electronic equipment is fitted on the nanopositioning table of our setup, under the AFM head; (b) Time-lapsed phase resonance curves before droplet deposition and during the evaporation process.
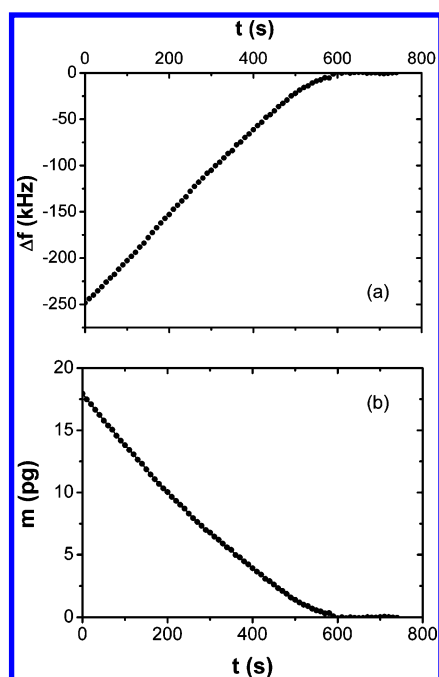
Figure 7. (a) Plot of the frequency extracted from the resonance curve shift as a function of time; (b) Evaporation curve giving the droplet mass as a function of time, obtained using the calibration function deduced from Figure 3.

increases until it reverses to the value of the empty resonator as the evaporation proceeds. In the results presented below, the acquisition time for one resonance curve was 10 s. This value was chosen as the best compromise between a short acquisition time and a sufficient number of points to have a precise description of the resonance curve.

The value of the resonance frequency was determined automatically by extracting the minimum of each resonance curve using dedicated control software. The plot of the frequency shift as a function of time (Figure 7a), was converted into an evaporation curve (Figure 7b) by applying the calibration function determined with silica beads on the same QBR. The essential need of the calibration process is illustrated when comparing these two curves. Indeed, in the initial stage of the evaporation, the slight increase of the slope observed on the frequency shift curve is entirely due to the saturation of the QBR response for larger loaded mass. Once the calibration nonlinearity is taken into account, the evaporation curve exhibits a monotonic variation of the slope, even at larger mass load.

This entire process was repeated, changing only the deposition contact time, to cover a large range of initial droplet sizes.

3. Results and Discussion

3.1. Glycerol Evaporations Curves. The evaporation curves measured on droplets with varying initial sizes are reported on Figure 8. The largest droplet, with a diameter of about 5 μm, covered nearly the whole surface of the QBR, whereas the smallest one was almost invisible with the AFM optical microscope. The initial masses ranging from 20 to 0.2 pg, with the corresponding volumes being between 15 fL and 150 aL, covered 2 orders of magnitude. The three curves obtained with initial masses of about 2 pg show the good reproducibility of the experiment.

In all cases, a smooth decrease of the mass with time was observed until complete evaporation of the droplet. Interestingly, the evaporation curve presented a nonlinear behavior for all the droplets, which means that the evaporation rate decreased with time during the process.

To get a better representation of the dynamics of evaporation over the large range of measurable masses, the same data are plotted in a logarithmic scale for the mass on Figure 8b. From this curve, the resolution of the mass-sensing device can be estimated to be better than 100 fg, as expected from the measured sensitivity (see Table 1). In our setup, the resolution is limited by the amplifier noise and by the presence of parasitic capacitance, both of which degrade the electrical signal. Even in this case, changes of resonance frequency in the kilohertz range can be detected. Improving the setup and the device layout should allow one to detect a smaller change of resonance frequency, approaching the limit given by the thermomechanical noise of the device. This confirms experimentally that the structure of the QBR was adequately designed for this study. In addition to this mass resolution, the smallest droplet also shows a limitation of the method in terms of time resolution. The short evaporation time did not allow the acquisition of a large number of complete resonance curves.

Finally, the relationship between the total evaporation time, τ, and the initial mass of the droplet can be compiled from all the collected data, as reported in logarithmic scale on Figure 9, which shows a well-defined power law with $\tau \propto m_0^{0.63 \pm 0.03}$.

3.2. Comparison with Macroscopic Models. The evaporation of sessile droplets has attracted a lot of attention. The classical descriptions[2-8] are based on a gas diffusion process. In this simple case, the mass loss derived from Fick's law is

Evaporation of Sessile Droplets

J. Phys. Chem. B, Vol. 111, No. 45, 2007 **13025**
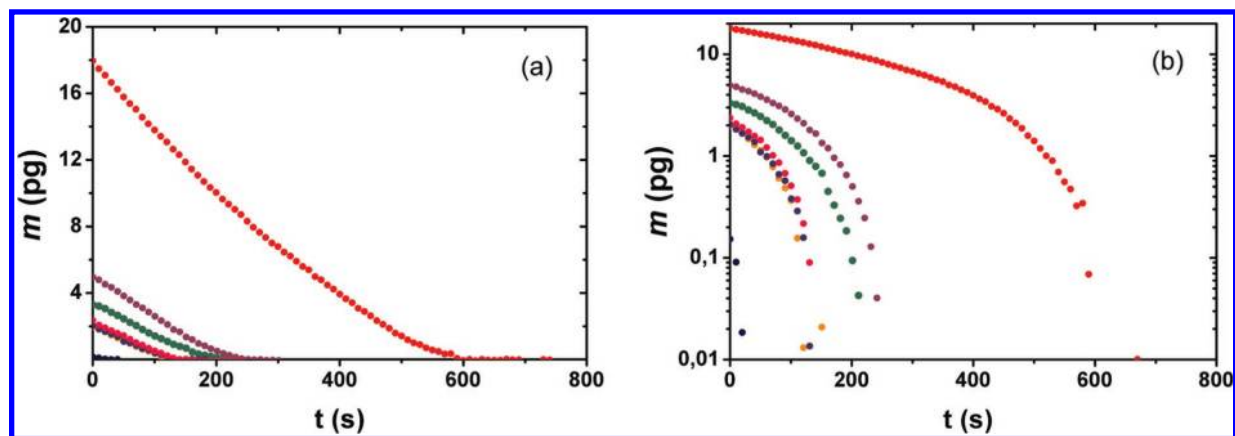
Figure 8. (a) Plots of the droplet mass versus time for six different droplets with initial volumes ranging from 150 aL to 15 fL. (b) Same data with masses represented in logarithmic scale.

given by

$$\frac{dm}{dt} = -4\pi Dr(c_s - c_\infty)f(\theta) \tag{5}$$

where m is the droplet mass; D is the diffusion coefficient of molecules in air; r is the contact radius of the drople; c_s and c_∞ are the molecule concentrations at the interface and at infinite distance, respectively; and $f(\theta)$ is a function of the droplet contact angle, θ. The same expression can be written using the saturated vapor pressure of the liquid, P_s, which is more easily accessible experimentally. This yields, in the case that $c_\infty = 0$,[8]

$$\frac{dm}{dt} = -\frac{4\pi DM}{RT}rP_s f(\theta) \tag{6}$$

where M is the molecular weight of the liquid, R is the universal gas constant, and T is the temperature. Several expressions were given for the $f(\theta)$ function. Using an electrostatic analogy, Picknett and Bexon[2] derived the exact form of this function. They provided empirical polynomial functions reproducing the exact solution with an error smaller than 0.2%. A simpler function provided by Bourges-Monnier and Shanahan[41] fits very well the exact solution for contact angles lying from 40 to 120°. It gives

$$f(\theta) = -\frac{\cos\theta}{2\sin\theta\ln(1 - \cos\theta)} \tag{7}$$

Using the relationship between m and r given by the spherical cap,

$$m = \frac{1}{3}\pi r^3 \rho(1 - \cos\theta)^2(2 + \cos\theta) \tag{8}$$

where ρ is the volumic mass of the liquid, one gets

$$\frac{dm}{dt} = -\alpha m^{1/3} \tag{9}$$

with

$$\alpha = \frac{4\pi DMP_s}{RT}f(\theta)\left(\frac{1}{3}\pi\rho(1 - \cos\theta)^2(2 + \cos\theta)\right)^{-1/3} \tag{10}$$

Generally, evaporation occurs following two basic modes: the constant radius mode, in which the base of the droplet remains pinned while the contact angle decreases with time, and the constant contact angle mode, in which the base shrinks while the contact angle remains constant. The first mode is observed on rather hydrophilic surfaces and the second one, on hydrophobic surfaces. Mixed modes with up to four regimes have also been reported.[41] Depending on the considered mode, solving eq 6 leads to different evaporation curves.

Optical observations of the evaporation process showed that the radius of the droplet deposited on QBR decreases with time, implying that the constant contact angle mode is dominating.

At constant contact angle, α remains constant during evaporation, and eq 9 is easily integrated, leading to

$$m^{2/3} = m_0^{2/3} - \frac{2}{3}\alpha t \tag{11}$$

The time evolution of the mass loss of the droplet is therefore nonlinear, in contrast to the constant radius mode, in which the decrease of mass is linear with time. The 2/3 power law was previously verified experimentally with large droplets in the microliter range.[2,5,9] It is important to note that the parameter α is entirely defined by (i) the liquid and surface properties and (ii) the experimental conditions. It does not depend on the droplet size.

To test the validity of the model down to femtoliter droplets, the experimental $m(t)$ curves were first fitted using eq 11 with α and m_0 as adjustable parameters. The fits obtained for four of the experimental curves are shown in Figure 10. For each droplet size, the match between eq 11 and the whole evaporation curve is excellent. From each of these curves, m_0 is unambiguously set by the initial droplet mass so that we can deduce univocally the value of the major fitting parameter α. We find $\alpha = 1.64 \pm 0.07 \times 10^{-10}$ g$^{2/3}$ s^{-1} for the whole set of curves with m_0 ranging from 0.16 to 18 pg. We therefore confirm that the fitting parameter α is independent of the initial droplet size.

The model can also be tested over the whole range of measured masses by comparing eq 11 to the experimental plot of $m_0^{2/3} - m^{2/3}$ as a function of t, in logarithmic scale (Figure 11). Remarkably, in this representation, all data coincide perfectly with a master straight line with a slope of 1 over 2 decades. The deduced value of α is identical to the one reported above.

Equation 11 also gives the total evaporation time, τ, of the droplet as a function of its initial mass, m_0: $\tau = 3/2\alpha m_0^{2/3}$ which is in very good agreement with the 0.63 $\pm$ 0.03 power law deduced from the experimental data reported Figure 9. The value of α determined using a 2/3 power law to fit the $\tau(m_0)$ data is $\alpha = 1.70 \times 10^{-10}$ g$^{2/3}$ s^{-1}, in agreement with the value reported above.

Proceeding further, the value of α can be related to physical properties of the system using the formula given by eq 10.
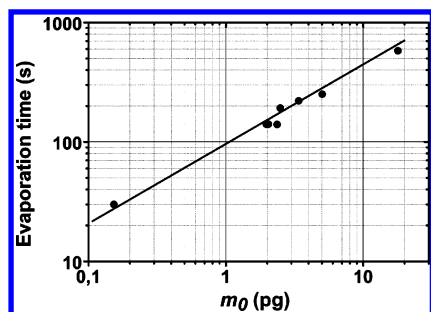
Figure 9. Plot of the total evaporation time, τ, of the droplet as a function of its initial mass. The slope of the linear fit is 0.63 ± 0.03.
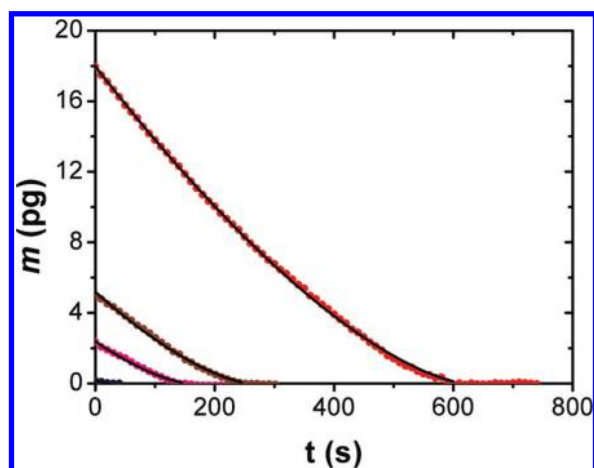

Figure 10. Fits of evaporation curves for various initial masses using eq 11.
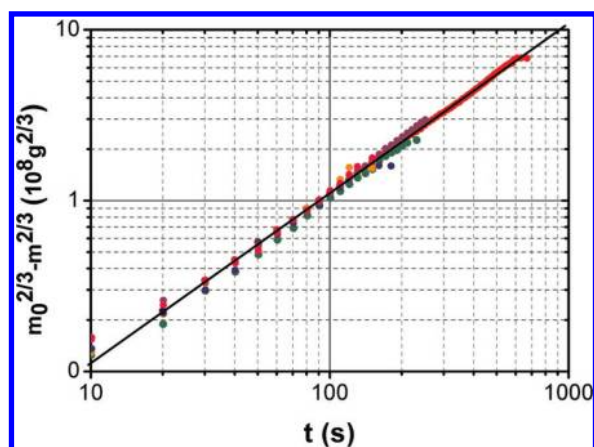

Figure 11. Logarithmic plot of $m_0^{2/3} - m^{2/3}$ as a function of t for the whole set of experimental curves.

Indeed, in this formula, most of the parameters can be measured directly or indirectly or are well-documented. The only unknown parameter is the diffusion coefficient, D, of glycerol in air. We therefore extracted an estimation of D from the present experimental data. The temperature measured on the AFM sample holder was 26 °C. The vapor pressure of glycerol as a function of temperature is well-documented in ref 42 and was taken as $P_s = 0.15$ mTorr. The contact angle θ of glycerol on the QBR surface cannot be determined directly. Nevertheless, the mass of each deposited droplet is known, and the radius of the droplets can be estimated by optical means. These data can be fitted using eq 8 with θ as an adjustable parameter. Despite the poor resolution of the radius determination, an estimate of the value of θ can be obtained; namely, $\theta = 60° \pm 5°$. Since this value lies in the domain of validity of eq 7, $f(\theta)$ can be computed and was found to be $f(\theta) = 0.416 \pm 0.008$.

Given all these parameters, the deduced value of D is $5 \pm 1 \times 10^{-2}$ cm^2 s^{-1}. To our knowledge, experimental measurements of this quantity are not available in the literature, but it can be compared with an estimate calculated using a model to predict any binary gas-phase diffusion coefficients.[43] The value extracted from this formula for glycerol in air is $D = 9 \times 10^{-2}$ cm^2 s^{-1}, which is in reasonable agreement with the value extracted from our experiment. Note that the value we found for glycerol is about 4 times smaller than the diffusion coefficient of water in air.

Altogether, these results show that the macroscopic constant angle model is appropriate to describe accurately the reported experiments, but the question of the limit of validity at small scale of the macroscopic model presented above becomes relevant. The main assumption of the model is that the evaporation process is driven by diffusion, which is sensible as long as the mean free path λ of the molecules in the vapor is smaller than the droplet dimensions (of radius r). This boundary is described by the dimensionless Knudsen number, Kn, given by the ratio of these two lengths: $Kn = \lambda/r$. It is usually assumed that evaporation is governed by the diffusion-controlled regime when the Knudsen number is smaller that 0.1.[2] For large Knudsen numbers, the evaporation regime is similar to the one observed in vacuum where the motion of molecules in the gas phase is ballistic. The evaporation rate is then given by the Hertz−Knudsen−Langmuir equation, which differs from eq 5.[44]

Assuming that λ is on the order of 0.1 μm in air, the droplet radius corresponding to $Kn = 0.1$ is ~1 μm, that is, a mass of 1 pg, which is within the limit of our mass sensing device. Hence, the diffusion controlled regime is justified for the droplets studied here except, maybe, for the smallest of all. Nevertheless, at this scale, the evaporation characteristic time approaches the acquisition time, and it is difficult to have enough points to detect a change of regime in the evaporation curves. Similarly, different evaporation regimes could be occurring at the very beginning (for example, constant contact area) or very end (for example, mixed constant area and constant angle) of the evaporation process without being detected. The resolution of the optics of the AFM is not sufficient to observe such minute variations, and in any case, such transient regimes would not lead to marked changes in the mass loss curves, as reported in ref 7. A precise monitoring of the contact angle during evaporation would be very useful but technologically difficult, since no experimental technique compatible with our droplet dispensing method allows noninvasive measurement on liquids at submicrometer scale.

Finally, other deviations from the macroscopic law could be considered in principle. For example, a significant increase in the Laplace pressure when the droplet size decreases should lead to a higher vapor pressure and so to a reduced evaporation rate. Unfortunately, currently available experimental techniques do not allow precise enough investigations of these effects, which should motivate the development of new methods with higher mass sensitivity and better time resolution.

4. Conclusions

In this paper, we have shown that the unique combination of ultrasensitive mass sensors with liquid nanodispensing techniques allows the study of evaporation droplets with diameters from the micrometer to submicrometer range, which correspond to volumes of femtoliters or smaller. These sizes are relevant for new methods of liquid manipulation developed for nanosciences where evaporation may play an important role. It is a

Evaporation of Sessile Droplets

J. Phys. Chem. B, Vol. 111, No. 45, 2007 **13027**

significant downsizing compared to most published data on microliter range and even with recent experiments in the 100 pL range.

Surprisingly, the macroscopic models based on diffusion-controlled process remain valid down to micrometer scale. It would be interesting to explore even smaller droplets, with dimensions comparable to the mean free path of molecules in air, ca. 100 nm, where the diffusion-controlled models should not be valid anymore.

Accordingly, the resonator should be operated at higher frequencies to improve its sensitivity according to eq 3. Another way of improvement is to use an alternative resonator design which would be more sensitive in terms of sensitivity to point mass accretion. An effect to take into account is that the evaporation time will be much shorter with nanometer-scale droplets. This will oblige the mass sensor to have a much faster response time. To circumvent this issue, new on-chip functions will be added as automatic tracking of resonance frequency with a phase lock loop (PLL) setup.

References and Notes

(1) Maxwell, J. C. *Collected Scientific Papers*; 1890; Vol. 11.

(2) Picknett, R. G.; Bexon, R. *J. Colloid Interface Sci.* **1977**, *61*, 336.

(3) Birdi, K. S.; Vu, D. T.; Winter, A. *J. Phys. Chem.* **1989**, *93*, 3702.

(4) Rowan, S. M.; Newton, M. I.; McHale, G. *J. Phys. Chem.* **1995**, *99*, 13268.

(5) Erbil, H. Y.; McHale, G.; Newton, M. I. *Langmuir* **2002**, *18*, 2636.

(6) Bourges-Monnier, C.; Shanahan, M. E. R. *Langmuir* **1995**, *11*, 2820.

(7) Kim, J. H.; Ahn, S. I.; Zin, W. C. *Langmuir* **2007**, *23*, 6163.

(8) Fang, X. H.; Li, B. Q.; Petersen, E.; Ji, Y.; Sokolov, J. C.; Rafailovich, M. H. *J. Phys. Chem. B* **2005**, *109*, 20554.

(9) Soolaman, D. M.; Yu, H. Z. *J. Phys. Chem. B* **2005**, *109*, 17967.

(10) Meric, R. A.; Erbil, H. Y. *Langmuir* **1998**, *14*, 1915.

(11) Hu, H.; Larson, R. G. *J. Phys. Chem. B* **2002**, *106*, 1334.

(12) Poulard, C.; Guena, G.; Cazabat, A. M. *J. Phys.: Condens. Matter* **2005**, *17*, S4213.

(13) Sirringhaus, H.; Kawase, T.; Friend, R. H.; Shimoda, T.; Inbasekaran, M.; Wu, W.; Woo, E. P. *Science* **2000**, *290*, 2123.

(14) Meister, A.; Liley, M.; Brugger, J.; Pugin, R.; Heinzelmann, H. *Appl. Phys. Lett.* **2004**, *85*, 6260.

(15) Fang, A. P.; Dujardin, E.; Ondarcuhu, T. *Nano Lett.* **2006**, *6*, 2368.

(16) Zimmermann, M.; Bentley, S.; Schmid, H.; Hunziker, P.; Delamarche, E. *Lab Chip* **2005**, *5*, 1355.

(17) Leng, J.; Lonetti, B.; Tabeling, P.; Joanicot, M.; Ajdari, A. *Phys. Rev. Lett.* **2006**, *96*.

(18) Deegan, R. D.; Bakajin, O.; Dupont, T. F.; Huber, G.; Nagel, S. R.; Witten, T. A. *Phys. Rev. E: Stat. Phys., Plasmas, Fluids, Relat. Interdiscip. Top.* **2000**, *62*, 756.

(19) Deegan, R. D. *Phys. Rev. E: Stat. Phys., Plasmas, Fluids, Relat. Interdiscip. Top.* **2000**, *61*, 475.

(20) He, J. Z. Q.; Gupta, S.; Emrick, T.; Russell, T. P.; Thiyagarajan, P. *Small* **2007**, *3*, 1214.

(21) Fang, X. H.; Li, B. Q.; Petersen, E.; Seo, Y. S.; Samuilov, V. A.; Chen, Y.; Sokolov, J. C.; Shew, C. Y.; Rafailovich, M. H. *Langmuir* **2006**, *22*, 6308.

(22) Belaubre, P.; Guirardel, M.; Garcia, G.; Pourciel, J. B.; Leberre, V.; Dagkessamanskaia, A.; Trevisiol, E.; Francois, J. M.; Bergaud, C. *Appl. Phys. Lett.* **2003**, *82*, 3122.

(23) Joyce, M. J.; Todaro, P.; Penfold, R.; Port, S. N.; May, J. A. W.; Barnes, C.; Peyton, A. J. *Langmuir* **2000**, *16*, 4024.

(24) Pham, N. T.; McHale, G.; Newton, M. I.; Carroll, B. J.; Rowan, S. M. *Langmuir* **2004**, *20*, 841.

(25) Haschke, T.; Bonaccurso, E.; Butt, H. J.; Lautenschlager, D.; Schonfeld, F.; Wiechert, W. *J. Micromech. Microeng.* **2006**, *16*, 2273.

(26) Bonaccurso, E.; Butt, H. J. *J. Phys. Chem. B* **2005**, *109*, 253.

(27) Dohn, S.; Sandberg, R.; Svendsen, W.; Boisen, A. *Appl. Phys. Lett.* **2005**, *86*, 233501.

(28) Bao, M. H. *MicroMechanical Transducers*; Elsevier: Amsterdam, 2000.

(29) Tamayo, J.; Ramos, D.; Mertens, J.; Calleja, M. *Appl. Phys. Lett.* **2006**, *89*, 224104.

(30) Chen, G. Y.; Thundat, T.; Wachter, E. A.; Warmack, R. J. *J. Appl. Phys.* **1995**, *77*, 3618.

(31) Ramos, D.; Tamayo, J.; Mertens, J.; Calleja, M.; Zaballos, A. *J. Appl. Phys.* **2006**, *100*, 106105.

(32) Arcamone, J. *Integration of nanomechanical sensors on CMOS by nanopatterning methods*; Ph.D. Thesis, UAB/INSA: Barcelona, 2007.

(33) Arcamone, J.; van den Boogaart, M. A. F.; Serra-Graells, F.; Hansen, S.; Brugger, J.; Torres, F.; Abadal, G.; Barniol, N.; Perez-Murano, F. "Full-wafer integration of NEMS on CMOS by nanostencil lithography"; IEEE IEDM, 2006, San Francisco, CA.

(34) Arcamone, J.; Misischi, B.; Serra-Graells, F.; van den Boogaart, M. A. F.; Brugger, J.; Torres, F.; Abadal, G.; Barniol, N.; Perez-Murano, F. *IEEE Trans. Circuits Syst. II* **2007**, *54*, 377.

(35) Zhao, J. H.; Bridges, G. E.; Thomson, D. J. *J. Vac. Sci. Technol. A* **2006**, *24*, 732.

(36) Tilmans, H. A. C.; Elwenspoek, M.; Fluitman, J. H. J. *Sens. Actuators, A* **1992**, *30*, 35.

(37) Buks, E.; Yurke, B. *Phys. Rev. E: Stat. Phys., Plasmas, Fluids, Relat. Interdiscip. Top.* **2006**, *74*, 046619.

(38) Li, M.; Tang, H. X.; Roukes, M. L. *Nat. Nanotechnol.* **2007**, *2*, 114.

(39) Yang, Y. T.; Callegari, C.; Feng, X. L.; Ekinci, K. L.; Roukes, M. L. *Nano Lett.* **2006**, *6*, 583.

(40) Ondarcuhu, T.; Nicu, L.; Cholet, S.; Bergaud, C.; Gerdes, S.; Joachim, C. *Rev. Sci. Instrum.* **2000**, *71*, 2087.

(41) Bourges-Monnier, C.; Shanahan, M. E. R. *C. R. Acad. Sci. Series II* **1993**, *316*, 311.

(42) Cammenga, H. K.; Schulze, F. W.; Theuerl, W. *J. Chem. Eng. Data* **1977**, *22*, 131.

(43) Fuller, E. N.; Schettler, P. D.; Giddings, J. C. *Ind. Eng. Chem.* **1966**, *58*, 18.

(44) Ray, A. K.; Lee, J.; Tilley, H. L. *Langmuir* **1988**, *4*, 631.